

# Ultra-compact integrated phase shifter via electrically tunable meta-waveguides

*Chengkun Dong<sup>1</sup>; Xiaowen Gu<sup>1,2,3</sup>; Yiyun He<sup>1</sup>; Ziwei Zhou<sup>1</sup>; Jiayi Wang<sup>1</sup>; Zhihai Wu<sup>1</sup>; Wenqi Wang<sup>1</sup>; Tangsheng Chen<sup>2,3</sup>; Jun Wu<sup>1</sup>; Tong Qiu<sup>1</sup>; Jun Xia<sup>1\*</sup>;*

1. Joint International Research Laboratory of Information Display and Visualization, School of Electronic Science and Engineering, Southeast University, Nanjing 210096, China

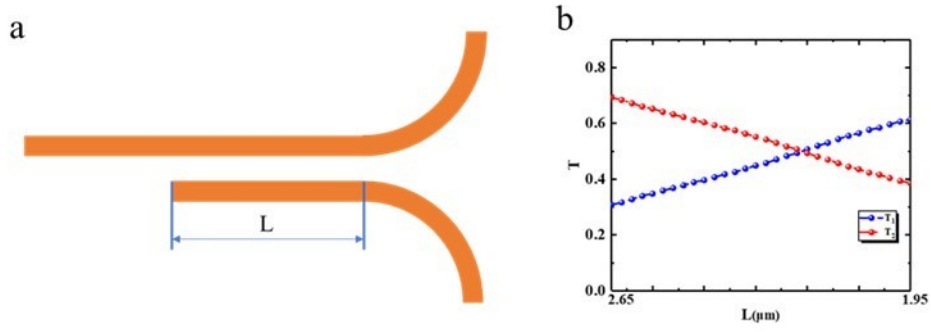
2. National Key Laboratory of Solid-State Microwave Devices and Circuits, Nanjing 210000, China

3. Nanjing Electronic Devices Institute, Nanjing 210096, China

\*E-mail: xiajun@seu.edu.cn

## Optimization of Directional Couplers

In order to reduce the loss of straight waveguides and curved waveguides, the width of the bus waveguide is designed to be 500nm to reduce mode leakage. Since the width of the waveguide in the active region is 350nm, tapers are required to connect the bus waveguide to the active region waveguide. To split the light from the input waveguide into two and input them into the two arms of the MZI with equal power, we use a directional coupler<sup>1</sup>. The figure below shows the variation of the intensity of the two arms with different lengths of the directional coupler. From Fig. S2 (b), we use a coupling length of  $\sim 2.39\mu\text{m}$

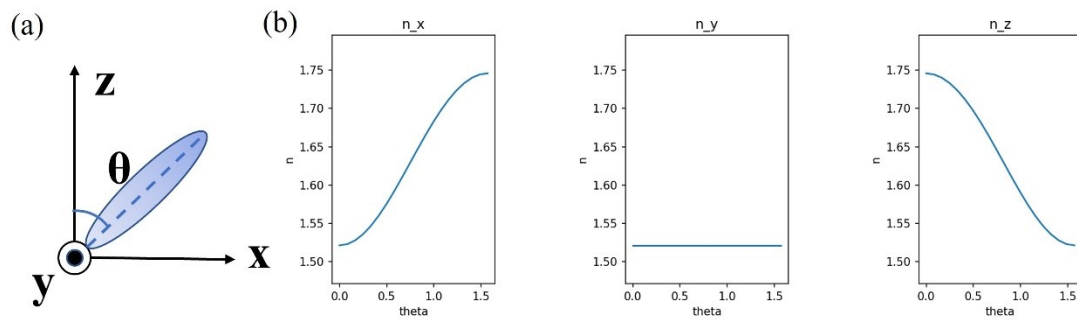


**Figure S1.** (a) Structure of directional coupler (b) Output optical intensity share of two ports versus coupling length

### Orientation of the liquid crystal

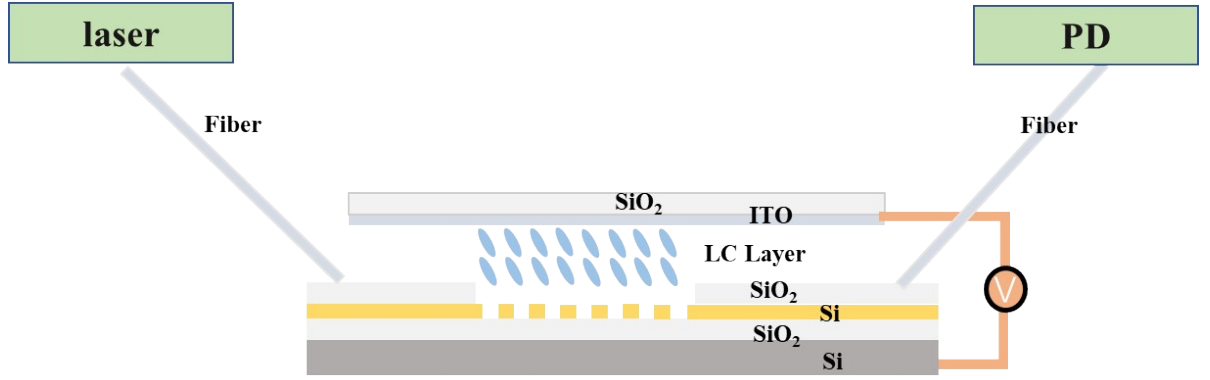
The orientation of the liquid crystal is initially parallel to the y-axis, and after applying a voltage, the liquid crystal will gradually be parallel to the z-axis as shown in the following Figure S2 (a).

The change in refractive index in different directions<sup>2,3</sup> ( $n_x$ ,  $n_y$ , and  $n_z$ ) are shown in the figure S2 (b).



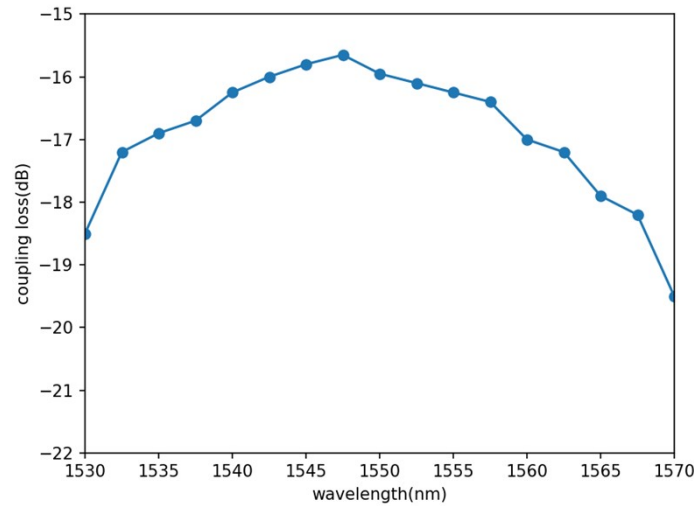
**Figure S2.** (a) Orientation of the liquid crystal. (b)  $n_x$ ,  $n_y$ , and  $n_z$  versus  $\theta$

### Powering method and optical testing method of the device.



**Figure S3.** Schematic diagram of device powering and optical testing.

The schematic diagram of power-on and light-on testing is shown in the figure, in which the input and output coupling gratings<sup>4</sup> (spectrum shown in Fig. S3) are located outside the liquid crystal packaging area for easy connection with optical fibers. The upper ITO glass is connected to the substrate with cured UV glue, which is prepared with micro-nano structures. The width of the coupling grating is about 10μm, which is matched with the core size of the single-mode fiber. The coupling gratings are connected to the bus waveguide by a taper.



**Figure S4.** Transmission spectrum of coupling grating

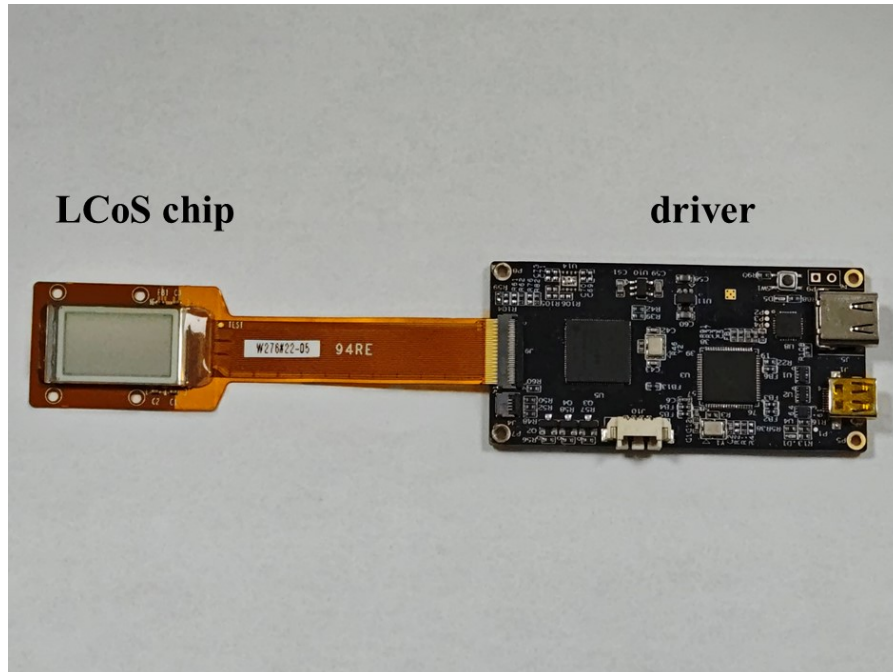
## Power consumption of LC meta-waveguide

Since the driving method of the proposed LC meta-waveguide is compatible with the existing Liquid Crystal On Silicon (LCoS) driving method, we measured the power consumption of a self-developed LCoS chip which has pixels of  $1920 \times 1080$  and the power consumption required for one pixel is calculated according to the following equation:

$$P_{lc\ meta-waveguide} = \frac{p_{lcos}}{N_{pixel}} \quad (1)$$

$$p_{lcos} = V_{drive} I_{drive} \quad (2)$$

Where  $N_{pixel} = 1920 \times 1080$ , and  $p_{lcos} \approx 22\ mW$ , which is the result of our test driving the entire chip. Therefore, it can be estimated that the power consumption of a single pixel is 10 nW. The driving method of the meta-waveguide is the same as that of the LCoS device. Therefore, it can be concluded that the power consumption of a single meta-waveguide phase shifter is also 10 nW.



**Figure S5.** Power consumption measurement of self-developed LCoS chip

## Network architecture

We incorporated two  $2 \times 2$  convolutional layers near the input layer, which were accelerated by the LCM-OCA. We trained this network on the CIFAR10 dataset and saved the model parameters when the cross-entropy loss function converged and the network achieved accurate classification on the test set. By modifying specific parameters, we accelerated parts of the network structure with the LCM-OCA. Our model has low complexity, fast computation and convergence speeds, and excellent performance on the classification task of the dataset. The performance of the modified model did not decrease after the parameter changes.

The CIFAR10<sup>5</sup> dataset is a ten-classification task dataset with 60,000 images, including 50,000 images in the training set and 10,000 images in the test set. Each image is a  $32 \times 32$  pixel color image with three channels of R, G, and B. Compared with the VGG16 network, our network structure is simpler, with model parameters about one-fourth of VGG16. This lightweight network structure is very suitable for low-resolution simple datasets, achieving accuracy similar to complex network models in a very short training time.

**Table S1** Architectural Details of the Network

Layer	Kernel	Num	Activation
Conv-1	$2 \times 2$	32	ReLU
Conv-2	$2 \times 2$	32	ReLU
Conv-3	$3 \times 3$	32	ReLU
Maxpool			
Other convolutional layers			
Maxpool			
FC-512	-	-	ReLU
FC-10			

The above table describes the layers of the network selected in our work, and we have used the optical convolutional processing unit to compute the first two convolutional layers of the network.

### Optimization of convolutional architecture.

We utilized various metrics to evaluate the similarity between different kernels. Our findings indicated that the Root Mean Square Error (RMSE) criterion demonstrated the most similar optimization trend to the kernels' feature extraction ability.

The RMSE is defined as follows:

$$RMSE = \sqrt{\frac{1}{n \times n} \sum_{j=1}^n \sum_{i=1}^n (y_{ij} - y'_{ij})^2} \quad (2)$$

Here, the 2x2 convolution kernel  $n=2$ ,  $y_{ij}$  represents the parameters of the convolution kernel in the saved model, and  $y'_{ij}$  represents the parameters in the kernel used for replacement. In addition to RMSE, we also employed other optimization functions such as Pearson correlation coefficient  $r$  and cosine similarity  $\cos(\theta)$  for kernel replacement.

$$r = \frac{\sum_{i,j=1}^n (y_{i,j} - \bar{y})(y'_{i,j} - \bar{y}')}{\sqrt{\sum_{i,j=1}^n (y_{i,j} - \bar{y})^2 \sum_{i,j=1}^n (y'_{i,j} - \bar{y}')^2}} \quad (3)$$

$$\cos(\theta) = \frac{Y \cdot Y'}{\|Y\| \cdot \|Y'\|} \quad (4)$$

Where  $Y$  and  $Y'$  are the 2x2 convolutional kernels in the saved model and the one used for replacement, and  $\bar{y}$  and  $\bar{y}'$  are their means. Our simulations show that the RMSE has

the closest optimization trend with the ability to extract features from kernels.

**Table S2** Convolutional Kernel Replacement Experimental Data Table


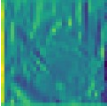
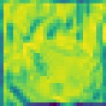
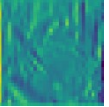
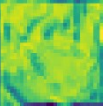
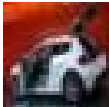
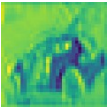
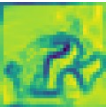
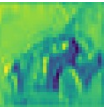
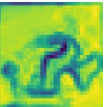

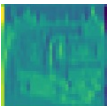
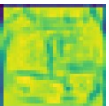
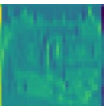
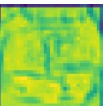
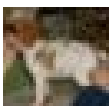
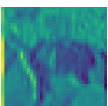
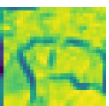
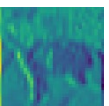
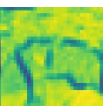
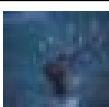
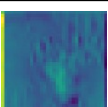
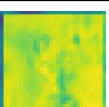
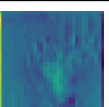
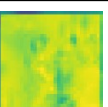
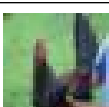
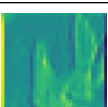
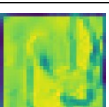
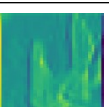
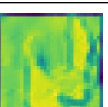
Optimization Function	Threshold	Success Rate on Conv-1	Success Rate on Conv-2	Accuracy on the Test Dataset
RMSE	0.05	100%	100%	91.80%
r	0.90	100%	100%	45.04%
$\cos(\theta)$	0.90	92%	90%	74.81%

Table S3 shows the input image and feature maps outputted by two 2×2 convolutional layers in a convolutional neural network<sup>6</sup>. The first column indicates the category of the input image, the second column shows the input image, the third and fourth columns show the feature maps outputted by the original first and second 2×2 convolutional layers, and the fifth and sixth columns show the feature maps outputted by the first and second 2×2 convolutional layers after replacing the convolutional kernels. (Note that the feature maps shown here are not normalized, and the actual input images in the network are normalized.)

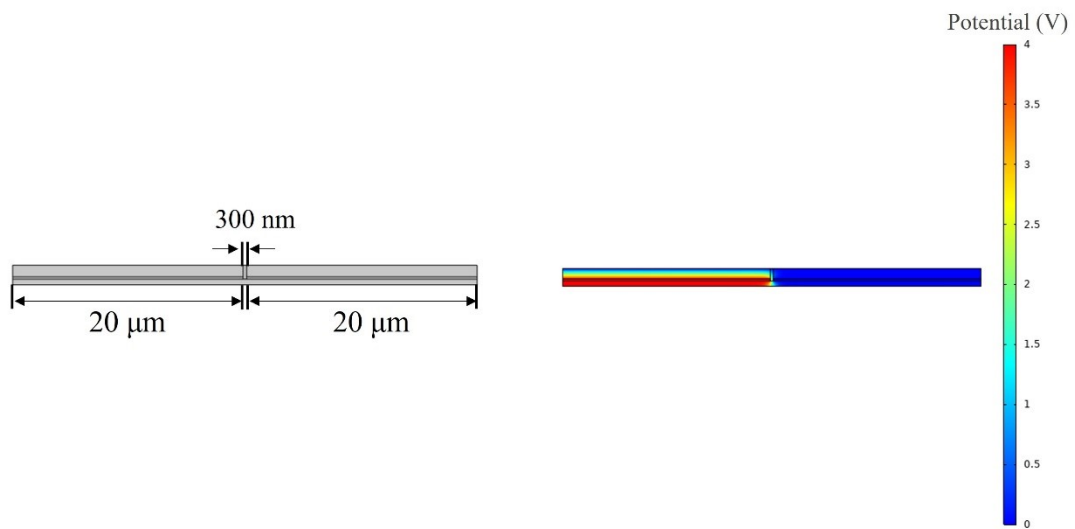
The figure below shows the results of applying optical convolutional processors to different types in the dataset<sup>7</sup>. The third and fourth columns represent the feature maps outputted by the original first and second layers of 2x2 convolutional layers, respectively. The fifth and sixth columns represent the feature maps outputted by the first and second layers of 2x2 convolutional layers after replacing the convolutional kernels.

**Table S3** the input image and the feature images outputted by two 2×2 convolution layers

class	input	conv2d_1	conv2d_2	conv2d_1	conv2d_2
-------	-------	----------	----------	----------	----------

frog					
car					
truck					
dog					
deer					
bird					

### Edge field effect simulation



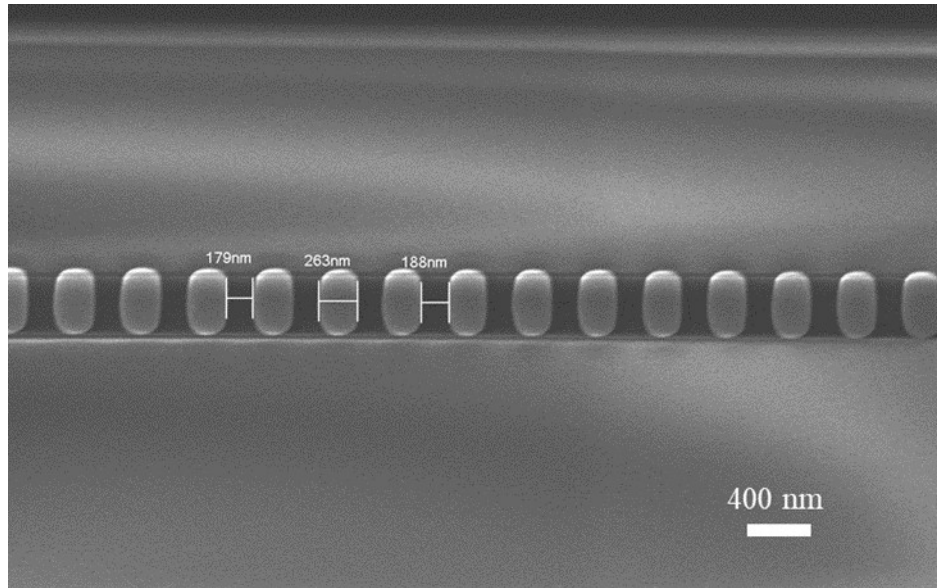
**Figure S6.** Edge field effect simulation (a) Simulation structure diagram; (b) Simulation results diagram

Large-scale integration needs to consider the edge field effect between pixels. Figure S6 a shows the simulation structure diagram, where the pixel size is 20 μm and the pixel pitch is 300 nm, with a dual-pixel structure. Figure S6 b shows the simulation results



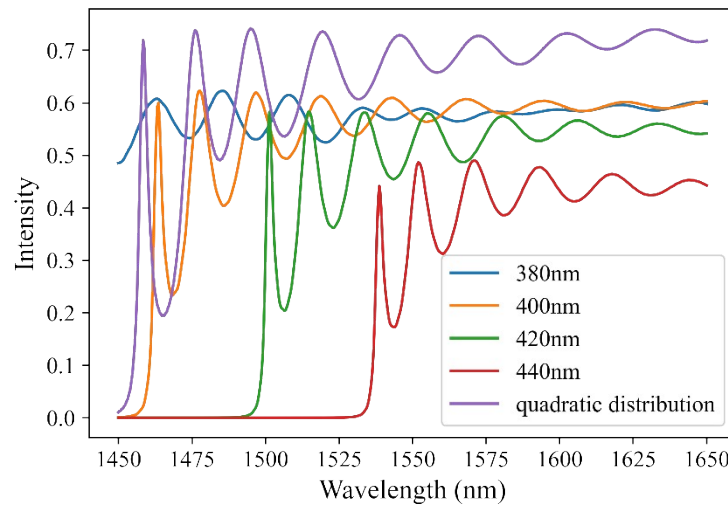
under applied voltage, where one pixel is set to a high potential and the adjacent pixel is set to a low potential. Due to the edge field effect, the edges of the low-potential pixel are influenced by the high-potential pixel, but the impact on the central region of the pixel is minimal, which is beneficial for large-scale integration.

### Structural details of meta-waveguides



**Figure S7** Zoomed-in view of the meta-waveguides.

### Comparison of Transmission for meta-waveguides with Different Sizes



**Figure S8** Simulation of Transmission Rates for Metawaveguides with Different Sizes. The

metawaveguides with equal spacing distribution have a width of 350nm, with periods of 380nm, 400nm, 420nm, and 440nm. The metawaveguides with quadratic distribution have a width of 350nm and a period of 400nm. It can be observed that the transmission of the metawaveguide with quadratic distribution is higher than that of the equal spacing distribution. This is because the quadratic distribution can better guide the optical field and minimizes scattered power from the meta-waveguides<sup>8</sup>.

## REFERENCES

- (1) Xu, P. P.; Zheng, J. J.; Doylend, J. K.; Majumdar, A. Low-Loss and Broadband Nonvolatile Phase-Change Directional Coupler Switches. *ACS Photonics* **2019**, *6*, 553-557.
- (2) Li, W. L.; Hu, X. M.; Wu, J. B.; Fan, K. B.; Chen, B. W.; Zhang, C. H.; Hu, W.; Cao, X.; Jin, B. B.; Lu, Y. Q.; et al. Dual-color terahertz spatial light modulator for single-pixel imaging. *Light Sci. Appl.* **2022**, *11*, 191.
- (3) Uchida, J.; Soberats, B.; Gupta, M.; Kato, T. Advanced Functional Liquid Crystals. *Advanced Materials* **2022**, *34*, 2109063.
- (4) Guo, R. X.; Zhang, S. J.; Gao, H. R.; Murugan, G. S.; Liu, T. G.; Cheng, Z. Z. Blazed subwavelength grating coupler. *Photonics Research* **2023**, *11*, 189-195.
- (5) Sun, Y. N.; Xue, B.; Zhang, M. J.; Yen, G. G. Completely Automated CNN Architecture Design Based on Blocks. *IEEE T. Neur. Net. Lear.* **2020**, *31*, 1242-1254.
- (6) Wu, S.; Wang, G. R.; Tang, P.; Chen, F.; Shi, L. P. Convolution with even-sized kernels and symmetric padding. In *33rd Conference on Neural Information Processing Systems (NeurIPS)*, Vancouver, CANADA, Dec 08-14, 2019; 2019; Vol. 32.
- (7) Anwar, S. M.; Majid, M.; Qayyum, A.; Awais, M.; Alnowami, M.; Khan, M. K. Medical Image Analysis using Convolutional Neural Networks: A Review. *J. Med. Syst.* **2018**, *42*, 226.
- (8) Ding, L.; Morits, D.; Bakker, R.; Li, S.; Eschimese, D.; Zhu, S. Y.; Yu, Y. F.; Paniagua-Dominguez, R.; Kuznetsov, A. All-Optical Modulation in Chains of Silicon Nanoantennas. *ACS Photonics* **2020**, *7*, 1001-1008.